ATMOSPHERIC SCIENCE

Increasing precipitation variability on daily-to-multiyear time scales in a warmer world

Wenxia Zhang[1], Kalli Furtado[2], Peili Wu[2], Tianjun Zhou[1,3,4]*, Robin Chadwick[2,5], Charline Marzin[2], John Rostron[2], David Sexton[2]

The hydrological cycle intensifies under global warming with precipitation increases. How the increased precipitation varies temporally at a given location has vital implications for regional climates and ecosystem services. On the basis of ensemble climate model projections under a high-emission scenario, here, we show that approximately two-thirds of land on Earth will face a "wetter and more variable" hydroclimate on daily to multiyear time scales. This means wider swings between wet and dry extremes. Such an amplification of precipitation variability is particularly prominent over climatologically wet regions, with percentage increases in variability more than twice those in mean precipitation. Thermodynamic effects, linked to increased moisture availability, increase precipitation variability uniformly everywhere. It is the dynamic effects (negative) linked to weakened circulation variability that make precipitation variability changes strongly region dependent. The increase in precipitation variability poses an additional challenge to the climate resilience of infrastructures and human society.

INTRODUCTION

The hydrological cycle is intensifying as the climate warms, with global mean precipitation increasing by 1 to 3% per degree rise of surface air temperature, in balance with the atmospheric energy budget (*1*, *2*). How the increased precipitation varies in space and time substantially affects regional climates and human societies (*3*–*5*). Over large spatial scales, climatologically wet regions will become wetter, while dry areas will become drier in the mean state, although this paradigm is less relevant to changes on land (*2*, *6*, *7*). Meanwhile, extreme precipitation will increase at a rate close to or even exceeding the moisture increase rate of 6 to 7%/K as dictated by the Clausius-Clapeyron relationship (*8*–*11*). The different rates of change in the mean and extreme precipitation suggest an altered temporal variation of precipitation. To fully understand the hydrological response, we need to look at the whole story, i.e., the full intensity distribution of precipitation across a range of time scales (*12*).

The statistical characteristics of precipitation and its future changes can be described using a probability density function (PDF) with respect to different intensity categories. Figure 1 illustrates three typical regimes featuring a monsoon climate (India), a midlatitude continental climate (Europe), and a tropical forest climate (the Amazon), from the perturbed physics ensemble (PPE) simulations [(*13*, *14*); see Materials and Methods]. Precipitation PDFs and their responses to global warming at different time scales are shown for illustration. The width of the PDF indicates—but does not exactly equal—the range of precipitation variability, and an expansion of the width suggests an increase in precipitation variability. The first regime (as the case in India; Fig. 1A and fig. S1, A to C) shows a shift and an extension of the PDF toward heavier precipitation in response to global warming. The second regime (as the case in southwestern Europe; Fig. 1B and fig. S1, D to F) is characterized by a mean decrease but with increased variability as indicated by a wider distribution. The third regime (as the case in Amazonia; Fig. 1C and fig. S1, G to I) features decreased and less variable precipitation, as indicated by a narrower distribution. The changes in precipitation variability, as seen through the widening or narrowing of the distribution, can substantially affect the occurrences and magnitudes of extreme events that lie in the tails of distributions (*15*). An increase in precipitation variability indicates wider swings between wet and dry conditions, exacerbating the risk of floods and/or droughts and possibly leading to rapid transitions between them (*3*). It is thus more difficult for societies to adapt to changes in variability than to changes in climate-mean states.

In contrast to the well-demonstrated changes in mean and extreme precipitation, changes in precipitation variability are less understood. Recent studies have suggested an increase in precipitation variability under future warming globally and in several continental regions over a range of time scales (*3*, *16*–*21*). To first order, the amplified precipitation variability has been hypothesized to primarily arise from the increasing moisture availability in the warmer atmosphere (*17*, *21*). In contrast, the weakening tropical atmospheric circulation under warming has been hypothesized to oppose the thermodynamic increases in precipitation variability (*16*, *18*). In particular, El Niño–Southern Oscillation (ENSO)–related circulation changes have been demonstrated to significantly affect interannual tropical Pacific precipitation variability (*22*). Nevertheless, a clear understanding of the mechanisms driving the increasing precipitation variability and how they play out from global to regional scales is lacking, prohibiting a comprehensive understanding of the hydrological responses to global warming. Thus, here, we apply a unified framework to explore the physical mechanisms underlying precipitation variability changes across time scales from daily to interannual.

RESULTS

Changes in regional precipitation variability under warming

We used a 14-member PPE of fully coupled simulations using the state-of-the-art climate model HadGEM3-GC3.05 [(*13*, *14*); see

[1]State Key Laboratory of Numerical Modeling for Atmospheric Sciences and Geophysical Fluid Dynamics, Institute of Atmospheric Physics, Chinese Academy of Sciences, Beijing, China. [2]Met Office, Exeter, UK. [3]CAS Center for Excellence in Tibetan Plateau Earth Sciences, Chinese Academy of Sciences, Beijing, China. [4]University of Chinese Academy of Sciences, Beijing, China. [5]Global Systems Institute, University of Exeter, Exeter, UK.
*Corresponding author. Email: zhoutj@lasg.iap.ac.cn

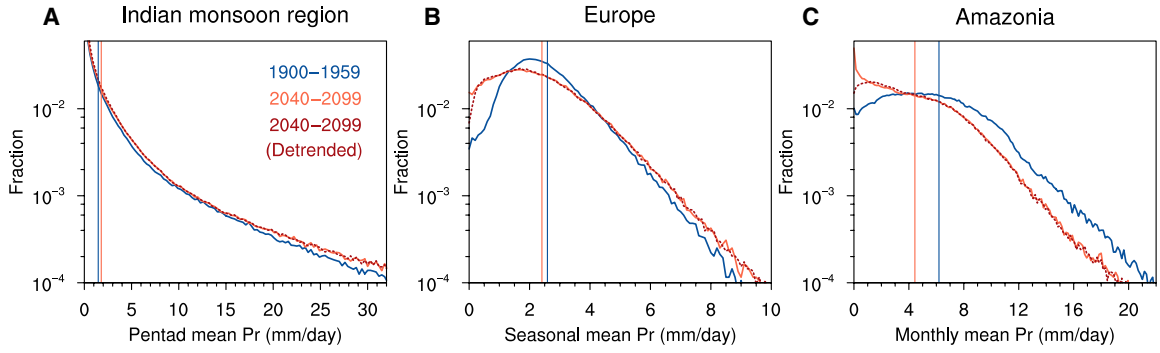

Fig. 1. Typical regimes of changes in precipitation distribution. (**A**) Pentad mean precipitation distribution in the Indian monsoon region (wetter and more variable), (**B**) seasonal mean precipitation distribution in southwestern Europe (drier but more variable), and (**C**) monthly mean precipitation distribution in Amazonia (drier and less variable) in the baseline 1900–1959 (blue) and 2040–2099 (pink for raw data and red for detrended data to exclude the influence of long-term trends in distribution). Precipitation distributions are calculated over the year and on model grid points before aggregating over the regions with an area weighting. Vertical lines denote climatological mean precipitation. The ensemble medians are shown. Definitions of the regions are shown as magenta boxes in Fig. 5B.

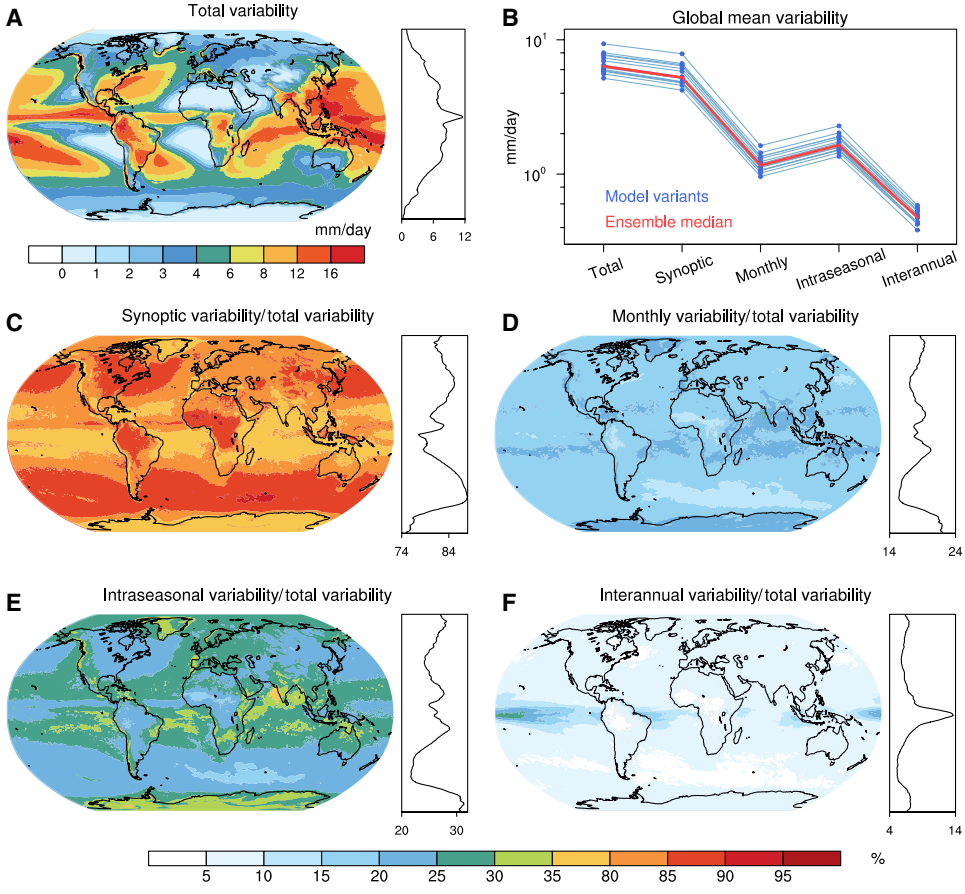

Fig. 2. Climatological precipitation variability and the relative importance of different time scales. (**A**) Total precipitation variability in the baseline 1900–1959 (mm/day). (**B**) Global area–weighted average precipitation variability, including total variability and variability on different time scales (mm/day). Blue and red curves represent model variants and the ensemble median, respectively. Note the logarithmic *y* axis. (**C** to **F**) Synoptic (C), monthly (D), intraseasonal (E), and interannual (F) precipitation variability as a percentage of total variability (%). The PPE ensemble medians are shown on the maps along with the zonal means.

Materials and Methods]. The different model variants—generated by perturbing the model parameters controlling key climate processes—sample a range of uncertainty in regional precipitation responses that is comparable to Coupled Model Intercomparison Project Phase 5 (CMIP5) (*14*). We considered precipitation variations at typical time scales from daily to interannual, including the synoptic (2 to 10 days), monthly (25 to 35 days), intraseasonal (30 to 80 days), and interannual (1 to 8 years) variations. The variability was estimated

as the standard deviation of the detrended and temporally filtered time series [(*16*, *17*); see Materials and Methods]. To investigate the response to warming, we compared precipitation variability between the first and last 60-year periods of the simulation, i.e., the baseline 1900–1959 and the projection in 2040–2099 under a high-emission scenario of Representative Concentration Pathway (RCP) 8.5.

The PPE ensemble reasonably reproduces the climatological mean and variability of precipitation at all time scales (fig. S2), which are well within the range of observations from IMERG [Integrated Multi-satellitE Retrievals for GPM; (*23*)] and GPCP [Global Precipitation Climatology Project; (*24*)] (with a pattern correlation exceeding 0.94 with IMERG for all time scales). Climatologically, the spatial distribution of precipitation variability resembles that of mean precipitation. Wet regions, such as the warm pool, equatorial Pacific, and monsoon regions, experience large variability (Fig. 2A). Across time scales, the magnitude of precipitation variability is large at the short synoptic time scale and small at the long interannual time scale (Fig. 2B). To indicate the relative importance of different time scales, we show precipitation variability at each time scale as a percentage of the total variability (Fig. 2, C to F). There exists a distinct latitudinal difference of the relative importance for each time scale. The synoptic variability is more prominent in extratropical storm tracks than in other latitudes, monthly and intraseasonal variability is more prominent in the tropics (related to Madden-Julian Oscillation and monsoon variability) and polar regions (related to snow/ice accumulation and melting) than in other latitudes, and interannual variability is more prominent at the equator (related to ENSO variability) compared to other latitudes. This reflects the dominant circulation regimes driving precipitation in different regions, which occur on different time scales.

As the climate warms, precipitation variability increases robustly over most of the globe, while decreases are confined to some subtropical subsidence regions mainly over the ocean (Fig. 3A). The increases in precipitation variability are generally stronger at shorter time scales in absolute terms (except for the slightly stronger increase in intraseasonal than monthly variability) (Fig. 3B and fig. S3). At the regional scale, the relative importance of different time scales in precipitation variability changes exhibits a consistent latitudinal structure with that in climatological precipitation variability (compare red and black curves in Fig. 3, C to F). This suggests the

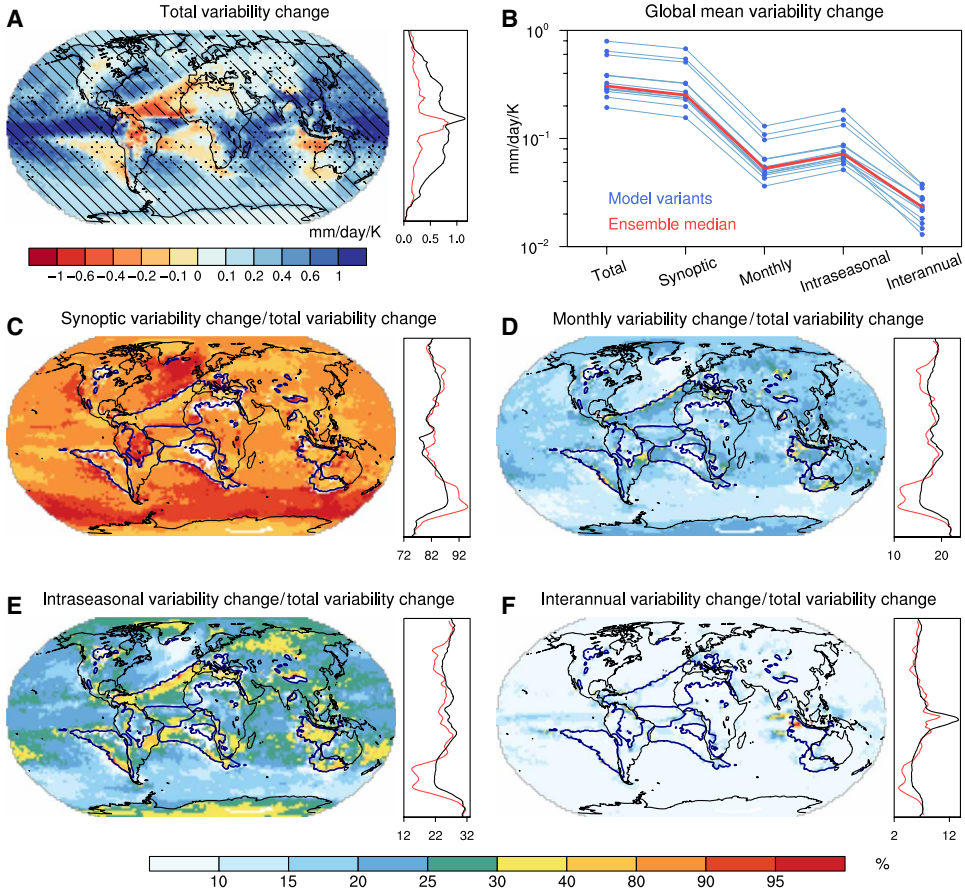

Fig. 3. Changes in precipitation variability and the relative importance of different time scales. (**A**) Projected changes in total precipitation variability (2040–2099 relative to 1900–1959) scaled with global mean temperature change (mm day^{-1} K^{-1}). Stippling (hatching) indicates regions where 80% (100%) of the model variants agree on the sign of change. (**B**) Global area–weighted average changes in precipitation variability, including total variability and variability on different time scales (mm day^{-1} K^{-1}). Blue and red curves represent model variants and the ensemble median, respectively. Note the logarithmic *y* axis. (**C** to **F**) Changes in synoptic (C), monthly (D), intraseasonal (E), and interannual (F) precipitation variability as a percentage of the total variability change (%). The ensemble medians are shown on the maps along with the zonal means (red for variability changes and black for climatological variability). Note that climatological zonal mean precipitation variability [i.e., the black curve in (A); in mm/day] is scaled by $^{1}/_{10}$ for clear display. Blue contours on (C) to (F) refer to where the total precipitation variability change equals zero.

importance of regional circulation regimes in precipitation variability changes. Precipitation variability amplifies across all seasons, with stronger increases in the local rainy season, such as boreal summer in the Northern Hemisphere and boreal winter in the Southern Hemisphere (fig. S4).

In terms of percentage changes, the responses in precipitation variability are markedly consistent across time scales, in both spatial distributions and magnitudes [with pattern correlations of 0.91 to 0.99 between different time scales for the ensemble medians; Fig. 4, A to D; also shown in (*16*)]. The global mean changes in precipitation variability are 4.85 to 5.70%/K (ensemble medians for the four time scales) with a peak near the equator. This rate is more than twice as fast as the increase in mean precipitation (ensemble median of 2.32%/K; Fig. 4, E and F).

At the global scale, analogous to the "wet-get-wetter" (*2*, *6*) pattern of mean precipitation change, the changes in precipitation variability can be approximately described as a "wet-get-more variable" pattern. Precipitation variability generally increases over climatologically wet regions, where precipitation climatology exceeds 50% of the global average (red contours in Fig. 4, A to D). Moreover, precipitation variability increases over a wider spatial extent than does mean precipitation (Fig. 4, A to E). To assess the applicability of the "wet-get-wetter" and "wet-get-more variable" paradigms at the regional scale, we compared changes in the mean state and variability of precipitation at grid points ranked from the driest to the wettest according to their precipitation climatology (Fig. 5A). To reduce spatial noise, we applied spatial smoothing first and show the probabilistic distributions of responses (see Materials and Methods). The wet-get-more variable paradigm applies well at the regional scale, with larger increases in variability expected at wetter locations (red in Fig. 5A). In contrast, the wet-get-wetter paradigm, which is expected from simple thermodynamic scaling, does not hold at the regional scale (black in Fig. 5A) (*25*). The direction of the mean precipitation change remains uncertain even for the wettest locations. This indicates substantial influences of the weakening in Walker circulation and spatial shifts in large-scale atmospheric circulations [related to, e.g., sea surface warming patterns, changes in land-sea temperature contrast, and relative humidity; (*2*, *7*, *25*, *26*)], which can modify and even dominate regional precipitation changes (*25*). This comparison suggests that, at the regional scale, the changes in precipitation variability (i.e., the wet-get-more variable paradigm) are less uncertain than the mean precipitation changes.

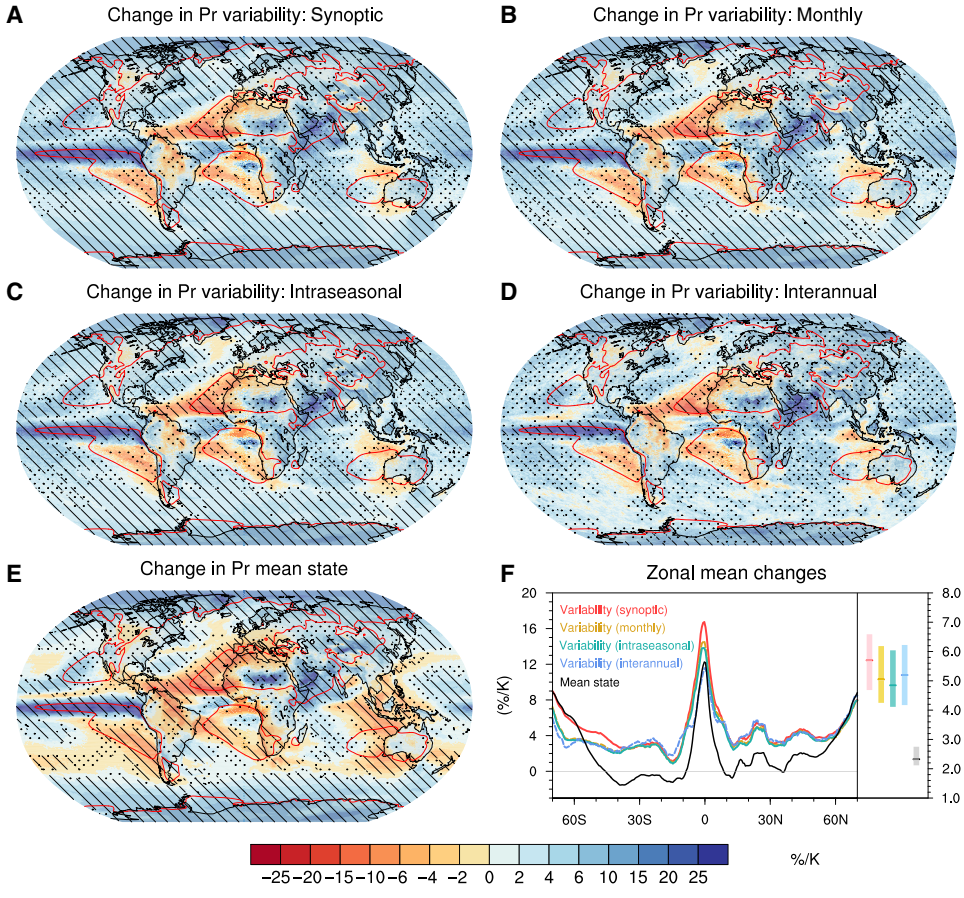

Fig. 4. Projected changes in precipitation variability. (**A** to **D**) Projected changes in precipitation variability at the synoptic (A), monthly (B), intraseasonal (C), and interannual (D) time scales. (**E**) Projected changes in mean precipitation. Changes are calculated for 2040–2099 relative to the baseline 1900–1959 under per degree of global warming (%/K). The ensemble medians are shown. Stippling (hatching) indicates regions where 80% (100%) of the model variants agree on the sign of change. The red contours indicate precipitation climatology exceeding 50% of the global average (i.e., 1.6 mm/day for the PPE), as a division of climatologically wet and dry regions. (**F**) Ensemble median zonal-mean changes in precipitation variability across time scales and mean precipitation (%/K). Bars show the global mean changes (ensemble median and 10th to 90th percentile spread).

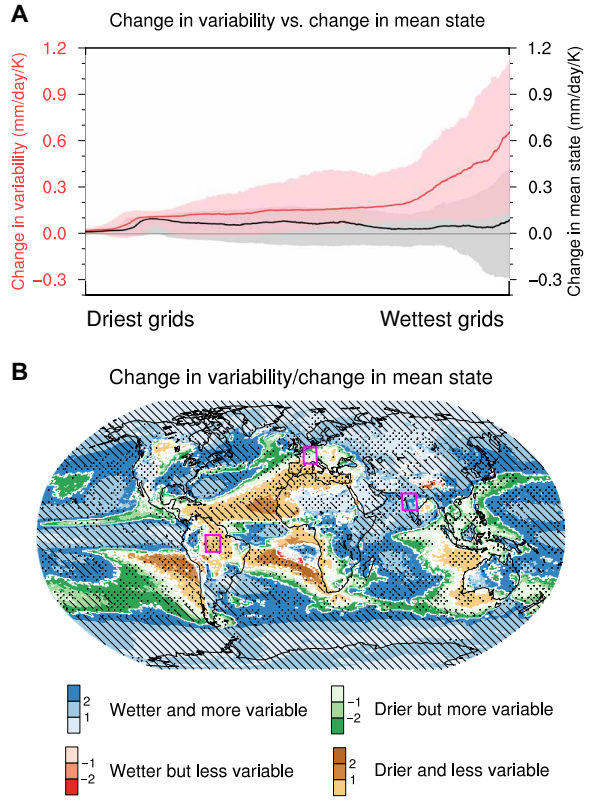

Fig. 5. Changes in precipitation variability versus mean precipitation. (**A**) Changes in the synoptic variability (red, left axis) and mean state (gray, right axis) of precipitation over the globe ranked from the driest to the wettest (*x* axis) according to baseline precipitation climatology. Changes are calculated for 2040–2099 relative to the baseline 1900–1959 under per degree of global warming (mm day^{-1} K^{-1}). The probabilistic distributions of the changes are derived by aggregating neighboring grids, with thick lines and shadings denoting the 50th and 10th to 90th percentile changes, respectively (see Materials and Methods). (**B**) Ratio of synoptic precipitation variability change to mean precipitation change, for the ensemble median. Stippling (hatching) indicates that at least 80% (100%) of the model variants agree on the classification. Magenta boxes (each at 10° × 10°) denote typical regimes of precipitation distribution change used for illustration in Fig. 1. The results are qualitatively consistent across time scales, and only those for synoptic variability are shown.

To this end, we can identify different regimes of precipitation responses based on the mean state and variability (Fig. 5B). Most of the globe (including approximately two-thirds of land) will face a wetter and more variable hydroclimate (blue in Fig. 5B). Over most of these regions, the percentage increase in precipitation variability is larger than the increase in mean precipitation. In the subtropical subsiding regions, both the "drier but more variable" and "drier and less variable" regimes are projected to occur, each covering ~16% of land. Over land, parts of southwestern Europe, southern Africa, central North America, and the Indo-China Peninsula will experience a drier but more variable hydroclimate, implying increased drought risks and less reliable freshwater resources (green in Fig. 5B). In contrast, the Mediterranean region and Amazonia are projected to experience a substantially weakened hydrological cycle with decreased and less variable precipitation (brown in Fig. 5B). A change in precipitation toward a wetter but less variable hydroclimate is less likely to occur (covering only ~3% of land). This classification of different regimes is valuable for regional adaptation planning, as different threats of hydrological extremes, water management, agriculture, and ecosystem services need to be tackled for different regimes.

Mechanisms driving precipitation variability changes

To understand the physical processes driving the changes in precipitation variability, we used moisture budget diagnostics [(*6*, *22*); see Materials and Methods]. We show that among all the moisture processes, the vertical moisture advection governs precipitation variations at all time scales, i.e.

$$P_f \approx \left(-\frac{\omega_m q_l}{g}\right)_f \quad (1)$$

where precipitation variations (P_f) can be approximated by the vertical advection of low-level moisture (q_l, 925-hPa specific humidity) by the mid-tropospheric vertical wind (ω_m, 500-hPa pressure velocity). The subscript f denotes variation at a specific time scale. The vertical moisture advection reasonably captures precipitation variability in the historical climate (figs. S5 and S6), as well as its changes under global warming (compare Figs. 4A and 6A, with a pattern correlation of approximately 0.75 for all time scales), particularly over climatologically wet regions.

To disentangle the roles of atmospheric moisture and circulation changes, i.e., thermodynamics and dynamics (*27*), we applied idealized models on the basis of Eq. 1 (see Materials and Methods). Specifically, the thermodynamic and dynamic contributions to the changes in Eq. 1 can be estimated by changing either moisture (q_l) or circulation (ω_m), respectively, to its future value while keeping the other quantity fixed to its baseline value. To first order, in terms of the percentage, the thermodynamic effect can be understood as the percentage change in the mean moisture availability ($\delta\bar{q}_l$), whereas the dynamic effect is linked to the percentage change in the variability of vertical motion ($\delta\sigma[-(\omega_m)_f]$), from simplifications by neglecting variations in humidity (see Eqs. 11 to 14 in Materials and Methods). The interaction between changes in moisture and circulation, referred to as the nonlinear term, is estimated as the residual between the total changes in the approximate vertical moisture advection (right-hand side of Eq. 1) and the thermodynamic and dynamic contributions estimated above.

The moisture budget processes driving precipitation variability changes are highly consistent in spatial patterns across time scales, albeit with differences in magnitudes (fig. S7). Here, we interpret the contributions of each term to precipitation variability changes, expressed as the percentage relative to climatological precipitation variability (Fig. 6 and figs. S8 and S9). The percentage contributions of each term to precipitation variability change are comparable across time scales. The thermodynamic effect, due to the increasing moisture availability under warming, intensifies precipitation variability globally with an overall spatially uniform magnitude (~5%/K averaged over wet regions; Fig. 6, B and C). In contrast, the dynamic effect, which is largely driven by the weakened variability of vertical motion, suppresses precipitation variability worldwide by ~3%/K, with a few regional exceptions, such as the equatorial Pacific (Fig. 6, D and E). Overall, this is consistent with the projected slowdown of the mean tropical circulation and a widening and poleward expansion of the subtropical subsidence zones as atmospheric stability increases in the future (*2*, *26*, *28*). In the mid to high latitudes, the reduced circulation variability is related to the decreased Northern

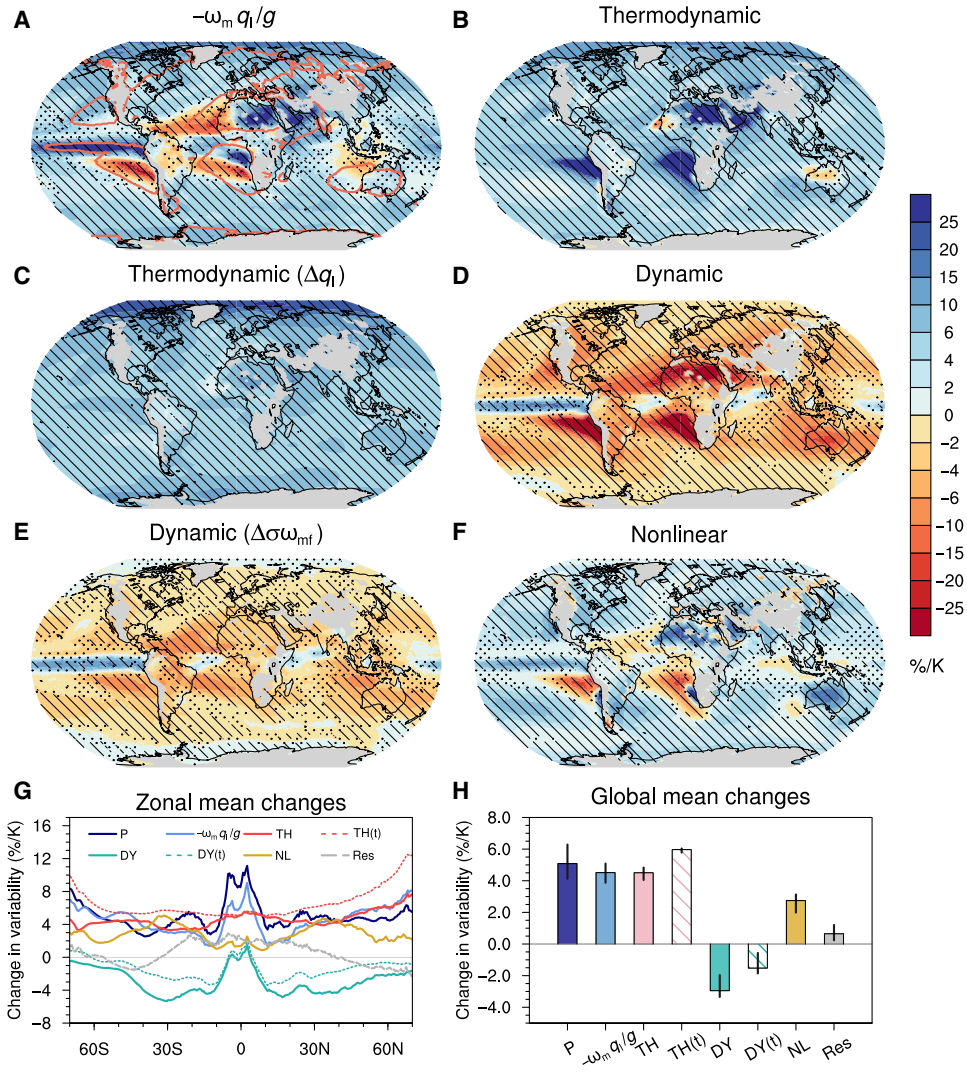

Fig. 6. Moisture processes driving changes in precipitation variability. (**A** to **F**) Changes in the variability of vertical moisture advection ($-\frac{\omega_m q_l}{g}$) (A) at the synoptic time scale, and its thermodynamic (TH) (B and C), dynamic (DY) (D and E), and nonlinear components (NL) (F). Each term is normalized by climatological precipitation variability and expressed in %/K. (C) and (E) show the theoretical estimates of TH and DY contributions, respectively, by neglecting variations in specific humidity (Eqs. 13 and 14 in Materials and Methods). The ensemble medians are shown. Stippling (hatching) indicates regions where 80% (100%) of the model variants agree on the sign of change. (**G**) Zonal and (**H**) global mean changes in the variability of precipitation (P), the vertical moisture advection, its TH, DY, and NL components, and the residual (Res) (%/K). TH(t) and DY(t) denote the theoretical estimates of thermodynamics and dynamics [i.e., corresponding to subplots (C) and (E)], respectively. Error bars in (H) denote the 10th to 90th percentile ensemble spread. Only the climatologically wet regions where the moisture budget approximation applies reasonably are included in the zonal and global means [outlined by red contours in (A); see Materials and Methods]. The results of moisture budget analysis are consistent across time scales; only those for synoptic variability are shown here (see figs. S8 and S9 for other time scales).

Hemisphere storm track activity as a result of the weakened baroclinic instability with the reduced meridional temperature gradient (*29*, *30*). In contrast to other regions, in the deep tropics, the dynamic contribution acts to enhance precipitation variability in the central-eastern equatorial Pacific (Fig. 6, D and E), which is in agreement with a deepening and narrowing equatorial convection zone with enhanced ascent under global warming (*28*, *31*). In the equatorial Pacific, the dynamic effects are likely linked to ENSO-related circulation changes, which are dominated by the spatially nonuniform sea surface warming and structural changes in ENSO-related sea surface temperature anomalies; these circulation changes intensify precipitation variability over the central-eastern Pacific but weaken precipitation variability over the western Pacific (*22*, *31*). We highlight that the dynamic effect determines the spatial structure of precipitation variability changes, including the peak increases near the equator and the weak changes in the subtropics (Fig. 6G) (*18*). In addition, the nonlinear term, i.e., covariations of moisture and circulation changes, further enhances precipitation variability (Fig. 6F). This is because large increases in moisture and updrafts tend to co-occur through latent-heating feedbacks in convection. The nonlinear term has a positive contribution globally, except over the subtropical descending regions, where convection is largely suppressed (Fig. 6, F to H). We note that within the warming level projected up to the end of the 21st century, precipitation variability and the associated

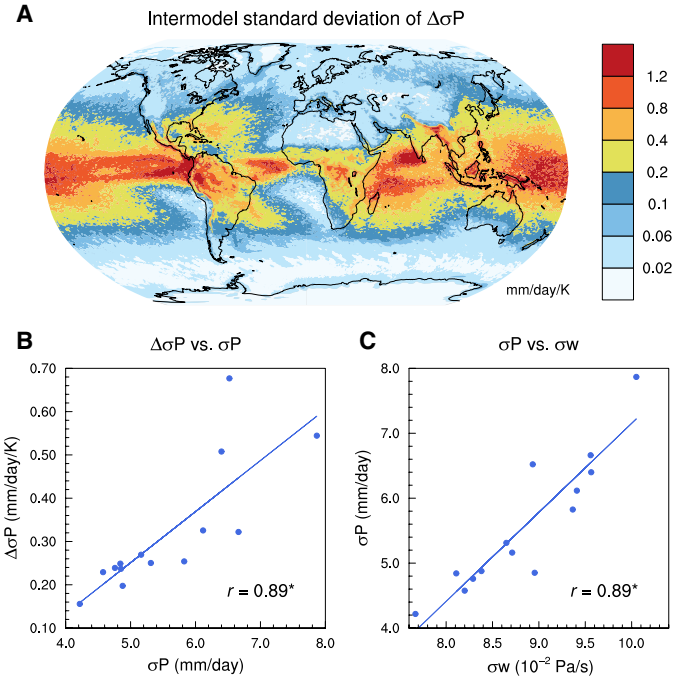

Fig. 7. Intermodel variant uncertainty in projected precipitation variability changes. (**A**) Intermodel variant standard deviation of precipitation variability changes (2040–2099 relative to 1900–1959; mm day^{-1} K^{-1}). (**B**) Scatterplot of global mean precipitation variability changes versus climatological precipitation variability. (**C**) Scatterplot of global mean climatological precipitation variability versus climatological ω500 variability. Dots denote individual model variants. Blue lines denote linear fits. The intermodel variant correlation is shown at the bottom, with asterisks indicating significance at the 0.05 level. The results are qualitatively consistent across time scales, and only those for synoptic variability are shown.

thermodynamic and dynamic components increase quasi-linearly, on average, over the globe with temperature increase (fig. S10).

Of particular importance is how these processes affect the wet and dry extremes, which are tightly related to the overall variability. Wet extremes are largely amplified by thermodynamics, with regional modulations from circulation changes (*11*, *27*). On the other hand, the increasing precipitation variability is also associated with increasing dry-day frequency and lengthened dry spells projected over many regions (e.g., over southwestern Europe in Fig. 1B) (*12*, *32*). This is thought to be related to enhanced convective inhibition, particularly over land, due to reduced low-level relative humidity under warming (*33*–*36*).

Intermodel variant uncertainty in precipitation variability projections

While precipitation variability is consistently projected to increase as the climate warms, the magnitude of the response varies substantially across model variants, particularly over tropical wet regions (Fig. 7A). At the global mean scale, the model spread in projected precipitation variability changes is predominantly related to the simulated climatological precipitation variability, which explains approximately 80% of the total intermodel variance (Fig. 7B). The intermodel scatter of simulated precipitation variability is further linked to that of circulation variability, as demonstrated in Eq. 12 (Fig. 7C). Hence, models with stronger climatological precipitation variability, likely associated with stronger circulation variability, tend to project larger increases in precipitation variability in terms of the absolute values. The significant intermodel relationship provides a potential for constraining projected precipitation variability changes. As a first step toward this constraint, specifically, the PPE model variants generally underestimate the present-day precipitation variability at a global scale compared to the IMERG observation (with the highest spatial resolution at present) (fig. S11). On the basis of the intermodel relationship identified here, this implies a potential underestimation of future precipitation variability changes by the PPE ensemble. A robust and formal constraint requires thorough investigation into the reliability and uncertainty of observed precipitation variability, which deserves dedicated research.

In addition to the above leading intermodel uncertainty mode, the large projection uncertainty in the tropics is also related to different sea surface warming patterns. For example, the intermodel scatter of the zonal gradient of precipitation variability changes between the central-eastern and western equatorial Pacific is related to that of sea surface warming, which is tightly associated with circulation changes (text S1 and fig. S12) (*22*, *31*). The zonal gradient of equatorial Pacific sea surface warming can be further traced back to different climatological precipitation biases in the tropical western Pacific via cloud-radiation feedbacks (fig. S12) (*37*).

This highlights the influences of climatological model biases and sea surface warming patterns on projected precipitation variability changes via different circulation responses. In particular, the implications for regional projections deserve dedicated research, as conducted in previous studies for regional precipitation projections (*37*–*39*). Thus, circulation changes are the key sources of uncertainty in many aspects of precipitation projections, including the mean (*40*–*42*), extremes (*10*, *11*), and variability associated with processes such as sea surface warming patterns and land-sea thermal contrast changes (*40*, *41*).

DISCUSSION

The increase in precipitation variability manifests the fact that global warming is making our climate more uneven—more extreme on both wet and dry conditions. With growing observational evidence pointing to increased occurrences of both floods and droughts from global to regional scales over the past century, it is necessary to examine whether an increase in precipitation variability has already emerged and, if so, the possible anthropogenic influence.

The resulting wider swings from one extreme to another will challenge the existing climate resilience of infrastructures, human society, and ecosystems. This makes climate change adaptation more difficult. As precipitation variability is projected to increase continuously with global temperature increases, international activities to reduce carbon emissions and limit global warming levels are urgently needed.

MATERIALS AND METHODS

Observational data

To validate the simulated precipitation variability, daily precipitation observations from IMERG [0.1° × 0.1°; (*23*)] and GPCP [1° × 1°; (*24*)] were used. We compared the present-day mean precipitation and precipitation variability over their common period of 2001–2019 (fig. S2). We note that precipitation intensity statistics, such as variability,

can be affected by horizontal resolution. For fair comparison, the higher-resolution IMERG data were regridded to the lower model resolution (N216) via area conservative remapping. The GPCP data were analyzed on its original grids. The comparison shows that the climatological mean and variability of precipitation simulated by the PPE ensemble are well within the range of observational uncertainty between IMERG and GPCP (partly related to their different horizontal resolutions; fig. S2).

Model simulations

We used the 14-member PPE simulations conducted with HadGEM3-GC3.05 developed by the Met Office Hadley Centre (*13*, *14*). HadGEM3-GC3.05 is a state-of-the-art coupled global climate model with a high resolution of N216 (60 km in the mid-latitudes) in horizontal and 85 levels in vertical. The ensemble members are generated by simultaneously perturbing 47 parameters controlling key processes in the atmosphere, land, and aerosol model components within expert-specified limits. The simulation includes historical simulations and RCP 8.5 projections from 1900 to 2099.

The different model variants in the PPE sample a range of uncertainty in regional precipitation responses that is comparable to CMIP5 despite sampling a relatively narrow range of global temperature changes (*14*). The advantage of using a single model framework is that the members all share a common structural bias so that emergent relationships across the PPE tend to be clearer than those in a multimodel ensemble, in which structural bias is an extra source of uncertainty. Different parameterizations across the PPE variants can lead to different precipitation and sea surface temperature biases and sea surface warming patterns, which are relevant for precipitation projections. Detailed physical understanding is not allowed in CMIP5/6 ensembles because of the unavailability of daily circulation data.

To investigate the response to global warming, we compared precipitation variability between the first and last 60-year periods of the simulation, i.e., the baseline 1900–1959 and the projection in 2040–2099, to maximize the signal-to-noise ratio in changes. The use of 60-year-long periods ensures sufficient sampling and, hence, reliable estimates of variability. The changes are scaled with global mean near-surface air temperature changes to eliminate the uncertainty of different warming rates across model variants. As precipitation variability increases quasi-linearly with global warming within the level projected up to the end of the 21st century, the scale provides a reasonable estimate of the response to warming (fig. S10).

Calculation of precipitation variability

We considered precipitation variations at typical time scales, including the synoptic variation at 2 to 10 days, the monthly variation at 25 to 35 days, the intraseasonal variation at 30 to 80 days, and the interannual variation at 1 to 8 years. The climatological annual cycle and linear trend were first removed from the time series before applying a filter according to the typical frequency for specific time scales. The variability was then estimated as the standard deviation of the filtered time series (*16*, *17*). The total precipitation variability was estimated as the standard deviation of the unfiltered time series.

Assessing "wet-get-more variable" at the regional scale

To assess the applicability of the "wet-get-wetter" and "wet-get-more variable" paradigms at the regional scale, we compared regional changes in mean precipitation and the variability (Fig. 5A). We ranked all the grid points globally from the driest to the wettest according to their precipitation climatology. To reduce spatial noise, we applied spatial smoothing before the sort by regridding to a coarser resolution (from ~60 to ~360 km; regridding to different resolutions is tested, which yields similar results). The changes in the variability and mean state of precipitation at each grid point were then sorted on the basis of their ranks in climatology. We interpret the changes in a probabilistic perspective by aggregating over the neighboring grids (301 grid points used here; slightly different aggregations are tested, which yield similar results) to derive a probabilistic distribution of changes. Then, we show the median change with the 10th to 90th percentile ranges (curve and shading in Fig. 5A). We performed the analysis for each model variant separately and then show the ensemble median results in Fig. 5A. Hence, the change patterns are examined in each of the model worlds, taking into account the potential differences in the distributions of wet and dry regions among different model variants.

For the wet-get-wetter paradigm, in addition to the precipitation-based ranks (Fig. 5A), we also examined the paradigm on the basis of ranks by precipitation minus evaporation ($P - E$; figure not shown). At the regional scale, the wet-get-wetter paradigm does not hold for either P or $P - E$, largely because of spatial shifts in convection and convergence in the tropics under future warming (*25*, *40*).

Moisture budget diagnostics

We applied the moisture budget diagnostics to investigate the physical processes driving the changes in precipitation variability. It has been widely used to diagnose changes in mean and extreme precipitation (*6*, *27*). In a climate state, precipitation (P) is balanced by evaporation (E) and vertical ($-<\omega\partial_p q>$) and horizontal ($-<\mathbf{V}\cdot\nabla q>$) moisture advection that are related to low-level convergence and horizontal winds, respectively

$$P - E = -<\omega\partial_p q> -<\mathbf{V}\cdot\nabla q> +\delta_0 \quad (2)$$

where q is specific humidity, ω is vertical velocity, $\mathbf{V}$ is horizontal wind vector, δ_0 is the residual, and $<\cdot> = \frac{1}{g}\int_{p_s}^{p_t}\cdot\, dp$ denotes vertical integral throughout the troposphere. Such a balance also holds at a specific time scale

$$P_f - E_f = -<\omega\partial_p q>_f - <\mathbf{V}\cdot\nabla q>_f + \delta_1 \quad (3)$$

where the subscript f denotes variation at a specific time scale derived from the filter.

Next, we applied simplifications to the full moisture budget to determine the moisture process that dominates the variation of precipitation and, based on which, to further understand the mechanisms for the projected changes.

First, among the moisture budget terms, the vertical moisture advection dominates precipitation variation at all time scales

$$P_f \approx -<\omega\partial_p q>_f \quad (4)$$

It largely captures the phase and magnitude of precipitation variation, as supported by the high temporal correlation (or explained variance) and low root mean square deviation (RMSD) with precipitation (fig. S6). Therefore, the vertical moisture advection reasonably reproduces the climatological precipitation variability (fig. S5)

Equation 4 involves the vertical moisture gradient and the integration of vertical moisture advection throughout the troposphere. It can be simplified by a two-layer model, where the difference in moisture in the lower (q_l) and upper (q_u) troposphere is used to approximate the vertical gradient of moisture

$$P_f \approx \left[-\frac{\omega_m(q_l - q_u)}{g}\right]_f \quad (5)$$

where ω_m represents the vertical motion at mid-troposphere, which is closely related to precipitation. As atmospheric moisture is concentrated in the lower troposphere, the right-hand side of Eq. 5 is dominated by its lower-level component. Hence, the variation in precipitation can be further approximated as that in the vertical advection of lower-level moisture

$$P_f \approx \left(-\frac{\omega_m q_l}{g}\right)_f \quad (6)$$

Here, ω_m is represented by mid-tropospheric vertical velocity at 500 hPa and q_l is represented by specific humidity at 925 hPa.

In terms of change, the vertical moisture advection reasonably reproduces changes in precipitation variability under global warming (comparing Figs. 4A and 6A)

$$\Delta\sigma[P_f] \approx \Delta\sigma\left[\left(-\frac{\omega_m q_l}{g}\right)_f\right] = \sigma\left[\left(-\frac{\omega_{m1} q_{l1}}{g}\right)_f\right] - \sigma\left[\left(-\frac{\omega_{m0} q_{l0}}{g}\right)_f\right] \quad (7)$$

where σ denotes variability (estimated by standard deviation) and Δ denotes the change between the baseline (1900–1959) and future (2040–2099), which are indicated by the subscripts 0 and 1, respectively.

We further separated the contributions from thermodynamics, dynamics, and nonlinear processes using idealized models. To estimate the thermodynamic (TH) contribution, which is related to changes in atmospheric moisture only, we change the specific humidity (q_l) to the future value and keep the circulation (ω_m) as in the baseline. The estimated changes in variability with this idealized model relative to the base period are regarded as the role of thermodynamics

$$TH \approx \sigma\left[\left(-\frac{\omega_{m0} q_{l1}}{g}\right)_f\right] - \sigma\left[\left(-\frac{\omega_{m0} q_{l0}}{g}\right)_f\right] \quad (8)$$

Likewise, for the dynamic (DY) contribution, which is due to changes in circulation only, we change the vertical velocity (ω_m) to the future value and keep the humidity (q_l) as in the baseline. Hence, the DY contribution is estimated as the changes in variability with this configuration relative to the baseline

$$DY \approx \sigma\left[\left(-\frac{\omega_{m1} q_{l0}}{g}\right)_f\right] - \sigma\left[\left(-\frac{\omega_{m0} q_{l0}}{g}\right)_f\right] \quad (9)$$

The nonlinear (NL) effect involves interactions between changes in humidity and circulation. It is estimated as the residual between the full changes in vertical moisture advection and the TH and DY contributions estimated from Eqs. 8 and 9

$$NL \approx \Delta\sigma\left[\left(-\frac{\omega_m q_l}{g}\right)_f\right] - TH - DY \quad (10)$$

To provide a theoretical understanding of the thermodynamic and dynamic effects, we investigated the moisture budget in a further simplified framework. As the variability in vertical motion is far larger than that in humidity, the variation in vertical moisture advection is largely governed by that in vertical motion. Hence, by neglecting the variation in humidity and its interaction with circulation, Eq. 6 can be simplified as follows

$$P_f \approx (-\omega_m q_l/g)_f \approx -\frac{(\omega_m)_f \overline{q_l}}{g} \quad (11)$$

where $\overline{q_l}$ is the climatological mean low-level humidity in a climate state. Thus, the variability in precipitation is proportional to that in vertical motion ($\sigma[-(\omega_m)_f]$)

$$\sigma[P_f] \approx \sigma\left[-\frac{(\omega_m)_f \overline{q_l}}{g}\right] = \frac{\sigma[-(\omega_m)_f]\overline{q_l}}{g} \quad (12)$$

Under this framework, the thermodynamic effect can be estimated as $\frac{\sigma[-(\omega_{m0})_f]}{g}(\overline{q_{l1}} - \overline{q_{l0}})$, which is determined by changes in atmospheric moisture and climatological circulation variability. The dynamic effect can be estimated as $\frac{\overline{q_{l0}}}{g}\{\sigma[-(\omega_{m1})_f] - \sigma[-(\omega_{m0})_f]\}$, which is determined by changes in circulation variability and climatological moisture availability.

The contributions of each term can be expressed as the percentage with respect to climatological precipitation variability, which then measures the direct contributions to the percentage precipitation variability change. The advantage is that the contributions of moisture and circulation changes are clearly separated between thermodynamics and dynamics

$$TH(t) \approx \frac{\left\{\frac{\sigma[-(\omega_{m0})_f]}{g}(\overline{q_{l1}} - \overline{q_{l0}})\right\}}{\left\{\frac{\sigma[-(\omega_{m0})_f]\overline{q_{l0}}}{g}\right\}} = \delta\overline{q_l} \quad (13)$$

$$DY(t) \approx \frac{\left\{\frac{\overline{q_{l0}}}{g}\{\sigma[-(\omega_{m1})_f] - \sigma[-(\omega_{m0})_f]\}\right\}}{\left\{\frac{\sigma[-(\omega_{m0})_f]\overline{q_{l0}}}{g}\right\}} = \delta\sigma[-(\omega_m)_f] \quad (14)$$

where $TH(t)$ and $DY(t)$ indicate the theoretical estimations of their contributions, respectively, and δ denotes a percentage change. To first order, the *TH* effect acts to enhance precipitation variability by the rate of background moistening (Eq. 13). The dynamic effect is associated with changes in the variability of vertical motion (Eq. 14).

While the simplified model in Eq. 11 has limitations in neglecting the variation in humidity and its interaction with circulation, it provides a clear understanding of the thermodynamic and dynamic contributions, which are solely related to moisture and circulation changes, respectively, in a percentage sense. As all the moisture budget terms are normalized by climatological precipitation variability, the percentage contributions of the thermodynamic, dynamic, and nonlinear components add up to explain the percentage precipitation variability changes.

To test the validity of this framework, we compared the phase and magnitude of variation between precipitation and vertical moisture

advection, which were indicated by temporal correlation (or explained variance) and RMSD between the filtered time series, respectively. Overall, the vertical moisture advection is a reasonable approximation of precipitation variation over climatologically wet regions, with an explained variance larger than 50% and RMSD less than 80% of the climatological precipitation variability (fig. S6). These regions correspond well to the climatologically wet regions with mean precipitation larger than 50% of the global average (see red contours in Fig. 6A and fig. S6). In particular, the simplified framework can better capture precipitation variability in the tropics than in the mid to high latitudes, with higher explained variance and lower RMSD in the tropics (fig. S6) (*22*). The high capability of the framework in the tropics has also been shown for annual-mean and seasonal-mean diagnosis (*40*, *41*, *43*). In subtropical descending regions where convection is largely suppressed, the variation in precipitation is not well explained by that in vertical moisture advection. Thereby, the quantitative contributions of moisture budget processes are estimated for these wet regions only.

One limitation of the moisture budget framework is that it cannot distinguish the causality between precipitation and evaporation changes. Given the much weaker changes in evaporation variability (with a global mean magnitude approximately 10% that of precipitation variability change; figure not shown), its contribution to precipitation variability change is believed to be small. Despite the aforementioned limitations mainly occurring on regional scales, on the global scale and particularly in the tropics, the moisture budget framework works reasonably well and explains 82 to 93% of global mean precipitation variability changes across different time scales.

SUPPLEMENTARY MATERIALS

Supplementary material for this article is available at http://advances.sciencemag.org/cgi/content/full/7/31/eabf8021/DC1

REFERENCES AND NOTES

1. M. R. Allen, W. J. Ingram, Constraints on future changes in climate and the hydrologic cycle. *Nature* **419**, 224–232 (2002).
2. I. M. Held, B. J. Soden, Robust responses of the hydrological cycle to global warming. *J. Climate* **19**, 5686–5699 (2006).
3. D. L. Swain, B. Langenbrunner, J. D. Neelin, A. Hall, Increasing precipitation volatility in twenty-first-century California. *Nat. Clim. Chang.* **8**, 427–433 (2018).
4. L. A. Gherardi, O. E. Sala, Effect of interannual precipitation variability on dryland productivity: A global synthesis. *Glob. Change Biol.* **25**, 269–276 (2019).
5. K. Sterle, B. J. Hatchett, L. Singletary, G. Pohll, Hydroclimate variability in snow-fed river systems: Local water managers' perspectives on adapting to the new normal. *Bull. Am. Meteorol. Soc.* **100**, 1031–1048 (2019).
6. C. Chou, J. D. Neelin, C. A. Chen, J. Y. Tu, Evaluating the "rich-get-richer" mechanism in tropical precipitation change under global warming. *J. Climate* **22**, 1982–2005 (2009).
7. M. P. Byrne, P. A. O'Gorman, The response of precipitation minus evapotranspiration to climate warming: Why the "wet-get-wetter, dry-get-drier" scaling does not hold over land. *J. Climate* **28**, 8078–8092 (2015).
8. K. E. Trenberth, Conceptual framework for changes of extremes of the hydrological cycle with climate change. *Clim. Change* **42**, 327–339 (1999).
9. R. P. Allan, B. J. Soden, Atmospheric warming and the amplification of precipitation extremes. *Science* **321**, 1481–1484 (2008).
10. P. A. O'Gorman, T. Schneider, The physical basis for increases in precipitation extremes in simulations of 21st-century climate change. *Proc. Natl. Acad. Sci. U.S.A.* **106**, 14773–14777 (2009).
11. S. Pfahl, P. A. O'Gorman, E. M. Fischer, Understanding the regional pattern of projected future changes in extreme precipitation. *Nat. Clim. Chang.* **7**, 423–427 (2017).
12. A. G. Pendergrass, D. L. Hartmann, Changes in the distribution of rain frequency and intensity in response to global warming. *J. Climate* **27**, 8372–8383 (2014).
13. D. M. H. Sexton, C. F. McSweeney, J. W. Rostron, K. Yamazaki, B. B. B. Booth, J. M. Murphy, L. Regayre, J. S. Johnson, A. V. Karmalkar, A perturbed parameter ensemble of HadGEM3-GC3.05 coupled model projections: Part 1: Selecting the parameter combinations. *Clim. Dyn.* **56**, 3395–3436 (2021).
14. K. Yamazaki, D. M. H. Sexton, J. W. Rostron, C. F. McSweeney, J. M. Murphy, G. R. Harris, A perturbed parameter ensemble of HadGEM3-GC3.05 coupled model projections: Part 2: Global performance and future changes. *Clim. Dyn.* **56**, 3437–3471 (2021).
15. R. W. Katz, B. G. Brown, Extreme events in a changing climate: Variability is more important than averages. *Clim. Change* **21**, 289–302 (1992).
16. A. G. Pendergrass, R. Knutti, F. Lehner, C. Deser, B. M. Sanderson, Precipitation variability increases in a warmer climate. *Sci. Rep.* **7**, 17966 (2017).
17. J. R. Brown, A. F. Moise, R. A. Colman, Projected increases in daily to decadal variability of Asian-Australian monsoon rainfall. *Geophys. Res. Lett.* **44**, 5683–5690 (2017).
18. C. He, T. Li, Does global warming amplify interannual climate variability? *Climate Dynam.* **52**, 2667–2684 (2019).
19. L. Dong, L. R. Leung, F. Song, Future changes of subseasonal precipitation variability in North America during winter under global warming. *Geophys. Res. Lett.* **45**, 12,467–12,476 (2018).
20. L. M. Alves, R. Chadwick, A. Moise, J. Brown, J. A. Marengo, Assessment of rainfall variability and future change in Brazil across multiple time scales. *Int. J. Climatol.* **41**, E1875–E1888 (2021).
21. A. A. Akinsanola, W. Zhou, T. Zhou, N. Keenlyside, Amplification of synoptic to annual variability of West African summer monsoon rainfall under global warming. *npj Clim. Atmos. Sci.* **3**, 21 (2020).
22. P. Huang, S.-P. Xie, Mechanisms of change in ENSO-induced tropical Pacific rainfall variability in a warming climate. *Nat. Geosci.* **8**, 922–926 (2015).
23. G. J. Huffman, D. T. Bolvin, D. Braithwaite, K. Hsu, R. Joyce, C. Kidd, E. J. Nelkin, P. Xie, NASA Global Precipitation Measurement (GPM) Integrated Multi-satellitE Retrievals for GPM (IMERG) (IMERG ATBD, version 4.5, 2015), 30 pp.;https://pmm.nasa.gov/sites/default/files/document_files/IMERG_ATBD_V4.5.pdf.
24. R. F. Adler, G. J. Huffman, A. Chang, R. Ferraro, P.-P. Xie, J. Janowiak, B. Rudolf, U. Schneider, S. Curtis, D. Bolvin, A. Gruber, J. Susskind, P. Arkin, E. Nelkin, The version-2 Global Precipitation Climatology Project (GPCP) monthly precipitation analysis (1979–Present). *J. Hydrometeorol.* **4**, 1147–1167 (2003).
25. R. Chadwick, I. Boutle, G. Martin, Spatial patterns of precipitation change in CMIP5: Why the rich do not get richer in the tropics. *J. Climate* **26**, 3803–3822 (2013).
26. G. A. Vecchi, B. J. Soden, Global warming and the weakening of the tropical circulation. *J. Climate* **20**, 4316–4340 (2007).
27. S. Emori, S. J. Brown, Dynamic and thermodynamic changes in mean and extreme precipitation under changed climate. *Geophys. Res. Lett.* **32**, L17706 (2005).
28. W. K.-M. Lau, K.-M. Kim, Robust Hadley circulation changes and increasing global dryness due to CO_2 warming from CMIP5 model projections. *Proc. Natl. Acad. Sci. U.S.A.* **112**, 3630–3635 (2015).
29. E. K. M. Chang, Y. Guo, X. Xia, CMIP5 multimodel ensemble projection of storm track change under global warming. *J. Geophys. Res.* **117**, D23118 (2012).
30. J. Lehmann, D. Coumou, K. Frieler, A. V. Eliseev, A. Levermann, Future changes in extratropical storm tracks and baroclinicity under climate change. *Environ. Res. Lett.* **9**, 084002 (2014).
31. S.-P. Xie, C. Deser, G. A. Vecchi, J. Ma, H. Teng, A. T. Wittenberg, Global warming pattern formation: Sea surface temperature and rainfall. *J. Climate* **23**, 966–986 (2010).
32. S. D. Polade, D. W. Pierce, D. R. Cayan, A. Gershunov, M. D. Dettinger, The key role of dry days in changing regional climate and precipitation regimes. *Sci. Rep.* **4**, 4364 (2014).
33. K. L. Rasmussen, A. F. Prein, R. M. Rasmussen, K. Ikeda, C. Liu, Changes in the convective population and thermodynamic environments in convection-permitting regional climate simulations over the United States. *Clim. Dynam.* **55**, 383–408 (2020).
34. J. Chen, A. Dai, Y. Zhang, K. L. Rasmussen, Changes in convective available potential energy and convective inhibition under global warming. *J. Climate* **33**, 2025–2050 (2020).
35. R. Chadwick, P. Good, K. Willett, A simple moisture advection model of specific humidity change over land in response to SST warming. *J. Climate* **29**, 7613–7632 (2016).
36. M. P. Byrne, P. A. O'Gorman, Understanding decreases in land relative humidity with global warming: Conceptual model and GCM simulations. *J. Climate* **29**, 9045–9061 (2016).
37. G. Li, S.-P. Xie, C. He, Z. Chen, Western Pacific emergent constraint lowers Projected increase in Indian summer monsoon rainfall. *Nat. Clim. Chang.* **7**, 708–712 (2017).
38. G. Li, S.-P. Xie, Y. Du, Monsoon-induced biases of climate models over the tropical Indian ocean. *J. Climate* **28**, 3058–3072 (2015).
39. X. Chen, T. Zhou, P. Wu, Z. Guo, M. Wang, Emergent constraints on future projections of the western North Pacific Subtropical High. *Nat. Commun.* **11**, 2802 (2020).
40. C. Kent, R. Chadwick, D. P. Rowell, Understanding uncertainties in future projections of seasonal tropical precipitation. *J. Climate* **28**, 4390–4413 (2015).
41. S.-M. Long, S.-P. Xie, W. Liu, Uncertainty in tropical rainfall projections: Atmospheric circulation effect and the ocean coupling. *J. Climate* **29**, 2671–2687 (2016).
42. T. G. Shepherd, Atmospheric circulation as a source of uncertainty in climate change projections. *Nat. Geosci.* **7**, 703–708 (2014).

43. R. Seager, N. Naik, G. A. Vecchi, Thermodynamic and dynamic mechanisms for large-scale changes in the hydrological cycle in response to global warming. *J. Climate* **23**, 4651–4668 (2010).

Acknowledgments
Funding: The study is jointly supported by the National Natural Science Foundation of China (41988101, 41905064), China Postdoctoral Science Foundation (2018M641450), the International Partnership Program of Chinese Academy of Sciences (134111KYSB20160031), and the UK–China Research Innovation Partnership Fund through the Met Office Climate Science for Service Partnership (CSSP) China as part of the Newton Fund. **Author contributions:** W.Z., K.F., P.W., and T.Z. designed the research. W.Z. performed the analyses and wrote the manuscript. D.S. and J.R. contributed model data. All authors contributed to interpreting the results and made substantial improvements to the manuscript. **Competing interests:** The authors declare that they have no competing interests. **Data and materials availability:** All data needed to evaluate the conclusions in the paper are present in the paper, the Supplementary Materials, and/or the linked repositories. The GPCP precipitation data are acquired from https://climatedataguide.ucar.edu/climate-data/gpcp-daily-global-precipitation-climatology-project. The IMERG precipitation data are acquired from https://gpm.nasa.gov/data/directory. For the HadGEM3-GC3.05 PPE simulations, two-dimensional fields can be accessed from https://catalogue.ceda.ac.uk/uuid/f1a2fc3c120f400396a92f5de84d596a, and post-processed three-dimensional fields can be accessed from https://doi.org/10.7910/DVN/GHWGG0.

Submitted 20 November 2020
Accepted 10 June 2021
Published 28 July 2021
10.1126/sciadv.abf8021

Citation: W. Zhang, K. Furtado, P. Wu, T. Zhou, R. Chadwick, C. Marzin, J. Rostron, D. Sexton, Increasing precipitation variability on daily-to-multiyear time scales in a warmer world. *Sci. Adv.* **7**, eabf8021 (2021).

Science Advances

Increasing precipitation variability on daily-to-multiyear time scales in a warmer world

Wenxia Zhang, Kalli Furtado, Peili Wu, Tianjun Zhou, Robin Chadwick, Charline Marzin, John Rostron and David Sexton

Sci Adv **7** (31), eabf8021.
DOI: 10.1126/sciadv.abf8021

Science Advances (ISSN 2375-2548) is published by the American Association for the Advancement of Science, 1200 New York Avenue NW, Washington, DC 20005. The title *Science Advances* is a registered trademark of AAAS.